

Hopping Transfer Optimizes Avalanche Multiplication in Molybdenum Disulfide

Xiaofan Cai[†], Ruichang Chen[†], Xu Gao[†], Meili Yuan[†], Haixia Hu[†], Hang Yin[†], Yuanyuan Qu^{†},
Yang Tan^{*†} and Feng Chen^{*†}*

*[†]School of Physics, State Key Laboratory of Crystal Materials, Shandong University, Shandong,
Jinan, 250100, China,*

E-mail: tanyang@sdu.edu.cn; drfchen@sdu.edu.cn; quyuanyuan@sdu.edu.cn

KEYWORDS: Avalanche multiplication, 2D material, Defect-engineer, Gas response.

ABSTRACT

Recently, avalanche multiplication has been observed in TMDC-based FETs, enhancing sensor performance with high sensitivity. However, the high voltage required for operation can damage the FETs, making it crucial to reduce the breakdown voltage for effective sensing applications. Here, we demonstrate that the utilization of hopping transfer induced by high-density defects can effectively reduce the breakdown voltage in TMDCs FETs. By substituting oxygen atoms for sulfur atoms in a monolayer of MoS₂, we create MoS_{2-x}O_x, with x carefully adjusted within the range of 0 to 0.51. Oxygen doping reduces the bandgap of TMDCs and enhances ion collision rates. Moreover, higher levels of oxygen doping ($x > 0.41$) in MoS_{2-x}O_x exhibit nearest-neighbor hopping behavior, leading to a significant enhancement in electron mobility. These improvements result in a decrease in the breakdown voltage of avalanche multiplication from 26.2 V to 12.6 V. Additionally, we propose avalanche multiplication in MoS_{2-x}O_x as an efficient sensing mechanism to overcome the limitations of gas sensing. The MoS_{2-x}O_x sensors display an ultra-high response to NO₂ gas in the air, with a response of 5.8×10^3 % to NO₂ gas of 50 ppb at room temperature, which is nearly two orders of magnitude higher than resistance-type gas detectors based on TMDCs. This work demonstrates that hopping transfer induced by high-density oxygen defects can effectively decrease the breakdown voltage of MoS_{2-x}O_x FETs, enhancing avalanche multiplication and serving as a promising mechanism for ultrasensitive gas detection.

INTRODUCTION

Transition metal dichalcogenides (TMDCs) have gained considerable attention as sensing materials for photo or gas detectors [1-4]. This is because of their unique structural characteristics, such as high specific surface area and strong surface adsorption capacity, as well as their excellent electronic properties, including high carrier mobility, good electrical stability, and tunable band gap [5-6]. Recently, the phenomenon of avalanche multiplication has been observed in TMDCs like MoS₂ and other two-dimensional TMDCs, attributing to the strong Coulomb interaction-induced quantum confinement effects [8-13]. Avalanche multiplication refers to a chain reaction process where charge carriers are accelerated by an external high voltage, leading to ionization of atoms through collisions. This generates additional carriers (electrons or holes) from the valence band [14-17]. By operating TMDC-based field-effect transistors (FETs) in an avalanche multiplication regime via gate-voltage modulation, weak signals induced by illumination or molecule adsorption can be amplified. The amplified signal through avalanche multiplication exhibits minimized background noise and ultrahigh sensitivity, enabling detectors to achieve exceptional performance [14,18]. There is a growing motivation to optimize and utilize carrier multiplication effects for photo/gas detection in order to achieve outstanding sensing performance.

The breakdown voltage (V_b) serves as a crucial parameter in avalanche multiplication-based detectors, which refers to the phenomenon of generating additional carriers through impact ionization [14,19-21]. It is highly desirable to minimize V_b , as excessively high values can lead to damage in TMDC-based FETs during repeated detection measurements. Extensive research has been carried out to investigate the influence of carrier type, TMDCs thickness, and length on avalanche multiplication [8,9,15,16]. It is currently believed that enhancing the collision probability of carriers per unit length (α) and reducing the TMDCs bandgap are effective strategies to reduce V_b [8,14]. Achieving these objectives require overcoming the inherent

limitations of pristine materials. In this context, the customized design and engineering of defects offer a highly promising approach.

Defects, such as vacancies and impurities, greatly affect the bandgap of TMDCs and can also cause carrier scattering due to random potential fluctuations [22-26]. However, defects in TMDCs also lead to carrier trapping and reduction of carrier mobility, hindering avalanche multiplication [27-30]. To address this contradiction, we propose the concept of hopping transfer between nearest-neighbor defects. Nearest-neighbor hopping (NNH) is a common phenomenon in polymers and materials with high defect concentrations, allowing for the generation of high carrier concentrations in defective materials [31-34]. To tackle this challenge, our research focuses on avalanche multiplication in MoS₂ with high defect concentrations.

In this work, we present the impact of NNH on the avalanche multiplication performance of MoS₂. By introducing oxygen (*O*) atoms to replace sulfur (*S*) atoms in a monolayer of MoS₂, we create defective structures known as MoS_{2-x}O_x, with *x* carefully controlled within the range of 0 to 0.51. When *x* exceeds 0.44, heavily doped *O* defects enable MoS_{2-x}O_x to exhibit NNH. Compared to pristine MoS₂, the presence of *O* defects in MoS_{2-x}O_x increases the collision probability of carriers, while maintaining a carrier mobility comparable to that of MoS₂. Remarkably, the NNH effect in MoS_{2-x}O_x leads to a higher susceptibility to avalanche multiplication compared to MoS₂, with a significant reduction in the breakdown voltage (*V_b*) from 26.2 V to 12.6 V under the same measurement conditions. Furthermore, we have developed a gas sensor utilizing the avalanche multiplication characteristics of MoS_{2-x}O_x. This avalanche multiplication sensor (MoS_{2-0.51}O_{0.51}) has a LOD of approximately 1.4×10⁻⁴ ppb and exhibits exceptional gas response to 50 ppb NO₂ gas at room temperature, with a remarkable signal responsivity of 5.8×10³%, surpassing traditional resistance-type gas detectors based on TMDCs by two orders of magnitude. Our MoS_{2-x}O_x gas sensor FETs operate based on the properties of avalanche multiplication, unlike conventional breakdown-type detectors that employ two parallel electrodes for gas ionization and breakdown voltage measurement [35-39].

Our sensor is versatile and suitable for gas concentration detection, particularly for low concentrations, as it does not require specific gas pressures. This work demonstrates the modulation of avalanche multiplication characteristics through hopping transfer and highlights avalanche multiplication as an efficient physical mechanism for the development of ultrasensitive gas sensors.

Preparation of MoS_{2-x}O_x FET

The monolayer MoS₂ film used in this study is synthesized using the chemical vapor deposition (CVD) technique. Supplementary I displays detailed characteristics of the MoS₂ monolayer. We transfer the MoS₂ film onto a pair of golden electrodes (*D* and *S*) with a separation distance of 10 μm (Fig. 1a). These electrodes are placed on a SiO₂/Si substrate, where the SiO₂ layer has a thickness of 300 nm, and the Si substrate is heavily doped with P⁺⁺ silicon. The contact quality of the MoS₂ film and electrodes is determined by the output curves (*I*_{DS}-*V*_{DS}) in Supplementary II. The forward *I*_{DS}-*V*_{DS} curve is displayed in a logarithmic scale and fitted following the equation $I_{DS}=C_0V_{DS}^\gamma$, where *C*₀ is a constant and γ is the parameter to quantify the average linearity of *I*_{DS}-*V*_{DS} curves [14]. In this situation, the γ is determined to be 0.90 ± 0.16 , demonstrating the non-perfect ohmic contact, as there are van der Waals gaps between MoS₂ film and Au electrodes generating the contact barrier.

O atoms are doped into the MoS₂ through a two-step process involving focused ion beam (FIB) irradiation and subsequent immersion in NO₂ gas (Fig. 1c). Initially, the focused Ga⁺ ion beam is utilized to sputter S atoms away from the outermost atomic layer of MoS₂ film, creating S vacancies (Fig. 1c(ii)) [40]. The ion beam energy is set at 30 keV, with varying beam currents of 7.7 pA, 24 pA, and 40 pA, respectively. To prevent any damage to the Mo atomic layer and the formation of holes in the MoS₂ structure, the irradiation time is carefully controlled to 500 ms. Subsequently, the irradiated film is immersed in NO₂ gas at the room temperature for 24 hours, allowing the Mo dangling bonds created by the irradiation to react fully with NO₂ (Fig.

1c(iii)). This reaction results in the substitution of *O* atoms for *S* vacancies, leading to the *O* doping of the irradiated film labeled as MoS_{2-x}O_x (Fig. 1c(iv)). To ensure that the FIB irradiation process not affect the contact between the MoS_{2-x}O_x film and gold electrodes, the irradiation area is limited to the region between the electrodes (Fig. 1b).

We determine the atomic ratio of the film after *O*-doping treatments using XPS (X-ray photoelectron spectroscopy) spectra (Fig. 1d-f) [41,42]. After the *O*-doping treatment, the elemental composition and atomic ratio of the sample undergo changes. The *S* atomic content gradually decreases with an increase in beam current, indicating that more *S* atoms are sputtered from the sample during FIB irradiation along with the enhanced beam current. Additionally, the peak at 236 eV gradually intensifies, corresponding to the bonding between *Mo* and *O*, demonstrating the successful incorporation of oxygen through the aforementioned process [41]. The measured atomic ratios (*x*) of *O:Mo* is 0.19(MoS_{2-0.19}O_{0.19}), 0.44 (MoS_{2-0.44}O_{0.44}) and 0.51 (MoS_{2-0.51}O_{0.51}), respectively, corresponding to beam currents of 7.7 pA, 24 pA, and 40 pA.

High conduction Hopping behavior in MoS_{2-x}O_x FET

Fig. 2a illustrates the transfer characteristics of MoS₂ and MoS_{2-x}O_x (*x* = 0.19, 0.44 and 0.51) at room temperature, presented in the logarithmic scale. The pristine MoS₂ exhibits the typical n-type behavior, with the on/off ratio ($V_{DS} = \pm 20$ V) of 3.7×10^5 . The field-effect mobility value (μ) for electrons is determined to be $10.74 \text{ cm}^2 \text{ V}^{-1} \text{ s}^{-1}$ by the equation $\mu = \frac{\partial I_{ds}}{\partial V_g} \frac{L}{WC_g V_{ds}}$, where *L* is the channel length; *W* is the channel width; *C_g* is the capacitance per unit area. Upon *O* doping, the on/off ratio and mobility of MoS_{2-x}O_x vary with *x*. Fig. 2b summarizes changes in mobility of MoS_{2-x}O_x corresponding to *x*. For *x* = 0.19, MoS_{2-0.19}O_{0.19} exhibits a reduced mobility of $0.02 \text{ cm}^2 \text{ V}^{-1} \text{ s}^{-1}$ with a decrease of nearly three orders of magnitude compared to MoS₂. The decreases in carrier mobility can be attributed to the low-density *O* defects in MoS_{2-0.19}O_{0.19}, which leads to self-trapping of carriers and random potential fluctuations. Therefore, the low-density *O* defects ultimately result in a decrease in both carrier mobility and on/off ratio.

As x increases to 0.51, the carrier mobility gradually increases to $5.39 \text{ cm}^2 \text{ V}^{-1} \text{ s}^{-1}$, approaching that of MoS_2 . We attribute this to higher O doping concentration, which leads to a short-range surface defects, thereby tailoring the carrier transport via the NNH of defect-induced localized states in the defective molybdenum disulfide [33].

The NNH can be confirmed by fitting the temperature dependent electric conductance (G) following equation:

$$G \propto \exp\left(-\frac{E_a}{k_b T}\right) \quad (1)$$

where E_a is the activation energy for hopping transport in 2D materials, k_b is the Boltzmann constant, and G is the conductance (I/V_{DS}) [31]. Fig. 2c illustrates the variation of I_{DS} - V_{GS} curves ($V_{DS}=3\text{V}$) for $\text{MoS}_{2-0.44}\text{O}_{0.44}$ (i) and $\text{MoS}_{2-0.51}\text{O}_{0.51}$ (ii) as the temperature increases from 310K to 510K. In Fig. 2d, we plot the temperature dependent G at $V_{GS}=20\text{V}$ and $V_{DS}=3\text{V}$. The linear fit of the logarithm of G ($\text{MoS}_{2-0.51}\text{O}_{0.51}$) as a function of T^{-1} provides a clear representation of a strong adherence to Equ. (1) and a conduction channel of the disordered molybdenum disulfide. This suggests that, at high temperatures, the variation in G with T corresponds to thermally activated NNH transport. Additionally, Supplementary III demonstrates the temperature-dependent behavior of G within the range of 220 K and 400 K, thereby confirming the conclusion regarding NNH transport.

We extract E_a from the thermally activated NNH model. Fig. 2e illustrates the relationship between E_a and V_{GS} , obtained by fitting the Arrhenius plot of the logarithmic of G and T^{-1} using Eq. (1). The decreasing E_a values for both $\text{MoS}_{2-0.44}\text{O}_{0.44}$ and $\text{MoS}_{2-0.51}\text{O}_{0.51}$ with increasing V_{GS} suggest the presence of multiple types of O traps [32]. Comparing the E_a values of $\text{MoS}_{2-0.44}\text{O}_{0.44}$ and $\text{MoS}_{2-0.51}\text{O}_{0.51}$, the higher value for $\text{MoS}_{2-0.51}\text{O}_{0.51}$ indicates that a higher concentration of O defects requires more energy for hopping transfer excitation.

Avalanche multiplication behavior in $\text{MoS}_{2-x}\text{O}_x$ FET

Fig. 3a demonstrates the forward I_{DS} - V_{DS} characteristics of the MoS_{2-x}O_x FET in the high V_{DS} region ($0 \text{ V} < V_{DS} < 40 \text{ V}$) with a fixed V_{GS} of 20 V. To prevent permanent damage to the sample due to repetitive testing, the scanning time for each I_{DS} - V_{DS} curve is limited to within 1 minute. The I_{DS} of the MoS₂ FET exhibits a sudden increase as V_{DS} increases (Fig. 3a), showing the typical carrier multiplication behavior at high voltages. The V_{DS} value at the point of I_{DS} mutation, known as V_b , is measured to be 26.2 V (Fig. 3b). As V_{GS} increases from 20V to 40V, the V_b of the MoS₂ FET gradually decreases (Fig. S4d). This contradicts the thermal breakdown variation caused by Joule heating, indicating that the observed carrier multiplication behavior is not a result of Joule heating but rather triggered by impact ionization under high electric fields [8,14]. The impact ionization process under high electric field conditions is illustrated in Fig. S4c. Under the influence of high V_{DS} , high-energy electrons (carriers) collide with n-type MoS₂, ionizing it and exciting additional electrons. These excited electrons continue to collide and ionize MoS₂ under the driving force of high V_{DS} , resulting in a chain reaction of avalanche multiplication. In this process, electron collision ionization plays a crucial role, and the impact ionization rate (α), as an important parameter for avalanche multiplication, can be determined by Equ. 2.

$$\alpha(V_{DS}) = \frac{1}{n} \frac{dn}{dx} = \frac{1}{L} \left(1 - \frac{1}{M}\right) \quad (2)$$

where n is the electron density [8,14,43,44]; L is the channel length (10 μm); M is the multiplication factor at $V_{DS} > V_b$ presented as $M(V_{DS}) = I_{DS}(V_{DS})/I_{DS}(V_b)$. Based on the above equation, we calculate the variation of α with V_{DS} , as shown in Fig. 3c.

In Fig. 3a, the MoS_{2-0.19}O_{0.19}, MoS_{2-0.44}O_{0.44}, and MoS_{2-0.51}O_{0.51} FETs also exhibit avalanche multiplication phenomenon in the high voltage range, and V_b and α show significant variations with different x values. Fig. 3c illustrates the variation of α with x . It is worth noting that α increases with increasing x , indicating a gradual increase in the probability of carrier collisions with higher defect concentration. First-principles calculations of the band structure of MoS₂₋

$x\text{O}_x$ are performed to further analyze the physical mechanisms of the impact ionization process influenced by O defect concentration in samples. As shown in Fig. 3d-3g, the bandgap of $\text{MoS}_{2-x}\text{O}_x$ gradually decreases with increasing x , from 1.67 eV ($x=0$) to 1.58 eV ($x=0.19$), 0.85 eV ($x=0.44$), and 0.55 eV ($x=0.51$). In the impact ionization process, high-energy carriers interact with bound electrons in the valence band through coulomb interactions. Based on the principles of energy and momentum conservation, high-energy carriers transfer energy to the bound electrons, causing them to cross the bandgap into the conduction band, resulting in carrier multiplication. As x increases, the reduction in the bandgap energy of $\text{MoS}_{2-x}\text{O}_x$ facilitates the transfer of excited electrons to the conduction band, thereby enhancing the likelihood of the impact ionization process.

Unlike α , the variation of V_b in $\text{MoS}_{2-x}\text{O}_x$ does not show a monotonic change with x . Instead, it initially increases to 28.4 V ($\text{MoS}_{2-0.19}\text{O}_{0.19}$) and then gradually decreases to 17.8 V ($\text{MoS}_{2-0.44}\text{O}_{0.44}$) and 12.6 V ($\text{MoS}_{2-0.51}\text{O}_{0.51}$) as shown in Fig. 3b. $\text{MoS}_{2-0.19}\text{O}_{0.19}$ has the highest V_b , indicating a difficulty in achieving avalanche multiplication. Although $\text{MoS}_{2-0.19}\text{O}_{0.19}$ has a higher α value compared to MoS_2 , suggesting a higher probability of collision-induced ionization by charge carriers, its mobility is significantly lower. As a result, the number of charge carriers available for collision ionization in $\text{MoS}_{2-0.19}\text{O}_{0.19}$ is lower than in MoS_2 at the same voltage, hindering the occurrence of avalanche multiplication. In contrast, $\text{MoS}_{2-0.44}\text{O}_{0.44}$ and $\text{MoS}_{2-0.51}\text{O}_{0.51}$ rely on the NNH mechanism for electron transport and maintain high mobility even with higher α values. Therefore, $\text{MoS}_{2-0.44}\text{O}_{0.44}$ and $\text{MoS}_{2-0.51}\text{O}_{0.51}$ are more likely to achieve avalanche multiplication.

Gas response of $\text{MoS}_{2-x}\text{O}_x$ avalanche FET

To investigate the gas response of MoS_2 and $\text{MoS}_{2-0.51}\text{O}_{0.51}$ FETs, we immerse them in a mixture of air and NO_2 gas and conduct repeated measurements of avalanche multiplication. With V_{GS} of 20 V, the concentration of NO_2 varies from 100 ppb to 250 ppb in increments of

50 ppb. The gas response of the MoS₂ FET is shown in Fig. 4a and Fig. 4b, where the output curves (I_{DS} - V_{DS}) of MoS₂ FETs are measured with V_{DS} ranging from 0 to 40 V (in steps of 0.2 V). The output curves exhibit noticeable differences in the avalanche multiplication behavior corresponding to different concentrations of NO₂ gas. As the NO₂ concentration increases from 100 ppb to 250 ppb, the avalanche multiplication factor α (at $V_{DS} = 35$ V) decreased from 496.9 cm⁻¹ to 151.5 cm⁻¹, while V_b increases from 27.3 V to 29.8 V (Fig. 4c). These results indicate that the presence of NO₂ gas suppresses avalanche multiplication.

To gain further insights, we performed first-principles calculations to investigate the charge transfer induced by the physisorbed NO₂ molecule on the adsorption site of MoS₂. The calculations revealed the extraction of electrons induced by the adsorption of NO₂ molecules. The NO₂ molecule possesses oxidizability due to the presence of unpaired electrons on the nitrogen atoms, which act as electron acceptors. As shown in Fig. 4d, the oxidative NO₂ molecule extracts electrons from the n-type MoS₂ channel, thereby reducing the carrier concentration in MoS₂. This reduced carrier concentration leads to a lower probability of impact ionization, which in turn requires higher electric fields to initiate avalanche multiplication in the NO₂-adsorbed MoS₂ monolayer.

We calculate the avalanche gas detection response (R_{AGD}) following the equation below:

$$R_{AGD}(V_{DS}) = \frac{|R_N(V_{DS}) - R_A(V_{DS})|}{|R_A(V_{DS})|} \times 100\% \quad (3)$$

where $R_N(V_{DS})$ and $R_A(V_{DS})$ represent the resistance of the MoS₂ FET with and without the NO₂ adsorption at the voltage of V_{DS} [45,46]. V_{DS} is selected to 35 V above the highest V_b in Fig. 4c, which ensures the occurrence of the avalanche multiplication under different NO₂ gas concentrations. Fig. 4e shows an average R_{AGD} of 2.2×10^2 %, 1.8×10^3 %, 3.6×10^3 %, and 4.6×10^3 %, corresponding to the NO₂ gas of 100 ppb, 150 ppb, 200 ppb, and 250 ppb, respectively. The measurement method of R_{AGD} is described in Supplementary V. The sensitivity of the MoS₂ FET, defined as the slope ($S = R_{AGD}/C$) of the resistance against NO₂

concentration (C), ranges from 2.2% to 18.5% per ppb within a concentration range of 100 ppb to 250 ppb.

The gas performance of MoS_{2-0.51}O_{0.51} FET is shown in Fig. 5a and Fig. 5b, which are I_{DS} - V_{DS} curves at $V_{GS} = 20$ V under the different gas atmospheres. When exposed to NO₂ gas, the device still exhibits avalanche multiplication behavior with V_b increasing from 13.8 V to 21.8 V along with the gas concentration increasing (from 50 ppb to 200 ppb) and α decreasing from 954.5 cm⁻¹ to 669.8 cm⁻¹ (Fig. 5c). Meanwhile, I_{DS} of the MoS_{2-0.51}O_{0.51} FET decreases for two orders of magnitude in the avalanche region ($V_{DS} > V_b$). The variation of I_{DS} is much more significant than the MoS₂ FET, demonstrating the MoS_{2-0.51}O_{0.51} FET is more sensitive to NO₂ gas than the MoS₂ FET.

Fig. 5d illustrates the calculated charge transfer of the NO₂ molecule on the adsorption site corresponding to the *O*-substituted configuration. Similar to the adsorption on the MoS₂ surface, NO₂ extracts electrons from the MoS_{2-0.51}O_{0.51} surface upon adsorption. As MoS_{2-0.51}O_{0.51} is a n-type semiconductor too, its charge carriers remain electrons. When NO₂ is adsorbed on the MoS_{2-0.51}O_{0.51} surface, it reduces the carrier density of MoS_{2-0.51}O_{0.51}. Fig. 5e shows the avalanche gas detection response of MoS_{2-0.51}O_{0.51} FET at V_{DS} of 35 V. The MoS_{2-0.51}O_{0.51} FET has ultra-high R_{AGD} of 5.8×10^3 %, 1.5×10^4 %, 2.2×10^4 %, and 3.3×10^4 %, corresponding to NO₂ gas of 50 ppb, 100 ppb, 150 ppb, and 200 ppb, respectively. It should be noticed that 50 ppb is the lowest NO₂ gas concentration that the mass gas flow controller (MFC) can accurately control in this work and is not the detection limit of the MoS_{2-0.51}O_{0.51} FET. Supplementary VI displays the avalanche behavior of the MoS_{2-0.51}O_{0.51} FET with the continuous decrease of the NO₂ concentration from 50 ppb over time, and distinct output curves are still observed at concentrations less than 50 ppb, indicating that the MoS_{2-0.51}O_{0.51} FET exhibits ultra-sensitivity to NO₂ molecules.

The limit of detection (LOD) is a crucial performance metric for gas sensors, representing the concentration of the analyte that produces a response three times higher than the noise level

of the device ($\text{LOD}=3\times\text{noise}/\text{sensitivity}$). Supplementary V displays the noise data of the measurement of 100 ppb NO_2 . An root-mean-square value of $\Delta R_{\text{AGD}}/R_{\text{AGD}}$ noise of approximately 0.7% is obtained, leading to a calculated LOD of approximately $3\times 0.7\%/(1.5\times 10^4\%/ppb)=1.4\times 10^{-4}$ ppb. Compared to resistive-type gas sensors, the avalanche-type gas sensor exhibits significantly higher sensitivity despite their higher noise levels, resulting in LOD values much lower than those of resistive-type ones.

Supplementary VII compares the gas-sensing response of our Avalanche-type sensors with reported resistance-type ones based on TMDCs, where the value of R_{AGD} is characterized consistently following Eq. (3). We divide TMDCs-based gas sensors into homostructure (green circle) and heterostructure (blue circle) according to the composition of materials. As one can see, the avalanche-type $\text{MoS}_{2-x}\text{O}_x$ FETs exhibit more significant gas-sensing performance than reported resistance-type sensors. In particular, the R_{AGD} of $\text{MoS}_{2-x}\text{O}_x$ FETs is two orders of magnitude greater than resistance-type ones, demonstrating that gas-sensing performances can be significantly improved by taking advantage of the avalanche multiplication.

Please note, the avalanche-type MoS_2 (or $\text{MoS}_{2-x}\text{O}_x$) FET has the same structural characteristic as the homostructure gas sensor except for the gas-detecting method (see [Experimental Methods](#) and [Fig. S5](#)). Traditional resistor-type detection typically performs measurements at a constant low operating voltage ($V_{\text{DS}} < 10$ V), and the gas adsorption (or desorption) modifies the current (or resistance) curve. In comparison, the avalanche-type one operates under a high impulse voltage ($V_{\text{DS}} > 20$ V) keeping itself in the avalanche regime, and the adsorbed (or desorbed) gas molecule disturbs the avalanche multiplication state intriguing a more drastic change in the current curve. Although the structure and materials of avalanche-type gas sensors are the same as the resistor-type ones, the gas-sensing performance of the avalanche-type TMDCs-based FET is greatly enhanced, demonstrating the advantage of the mechanism of avalanche multiplication.

Conclusion

Our work demonstrates the potential of using NNH to reduce the breakdown voltage of $\text{MoS}_{2-x}\text{O}_x$ FETs and enable ultrasensitive gas detection. By substituting O atoms for S atoms in a monolayer of MoS_2 , we make $\text{MoS}_{2-x}\text{O}_x$ with carefully controlled O doping levels. The high level of oxygen doping in $\text{MoS}_{2-x}\text{O}_x$ ($x > 0.41$) exhibit a NNH behavior, significantly enhancing electron mobility. Meanwhile, the O doping not only reduces the bandgap of TMDCs but also enhances ion collision rates. These improvement decreases the breakdown voltage of avalanche multiplication. We also propose avalanche multiplication in $\text{MoS}_{2-x}\text{O}_x$ is the promising option for ppb-level gas sensing, exhibiting a response of 5.8×10^3 % to NO_2 gas at 50 ppb concentration at room temperature, two orders higher than the resistance-type gas detectors based on TMDCs. This work highlights the effectiveness of hopping transfer induced by high-density oxygen defects in reducing the breakdown voltage of $\text{MoS}_{2-x}\text{O}_x$ FETs and enabling ultrasensitive gas detection, and opens up new possibilities for the development of highly sensitive gas sensors.

Experimental Methods

Sample preparation

The MoS₂ monolayers were grown on a SiO₂/Si substrate via the CVD method. After then, the MoS₂ was transferred to a SiO₂/Si substrate with prefabricated Au electrodes (Au: 50 nm, SiO₂: 300 nm) via a standard PDMS-Assisted Transfer Process [47]. A thin layer of PDMS was placed on top of MoS₂ on SiO₂/Si, the assembly was immersed into the 90 °C 2-mol/L KOH solution for 15 minutes to etch SiO₂ away. The sample was then taken out and rinsed three times with DI water. PDMS was peeled off from SiO₂ and adhered to the slide. Next, the PDMS was stamped on the target substrate via the transfer stage and thermally released at 80 °C. Finally, the assembled device was annealed in an argon-protected tube furnace at 200 °C.

Characterization

The fabricated devices were characterized using an optical microscope (Leica DM2700), and AFM (Bruker, Dimension Icon). The electrical characteristics were measured via Keithley 4200A-SCS at room temperature. The power of the laser used in Raman spectra measurements was 1mW, and the wavelength was 532 nm.

Gas-detecting Method

The gas sensing measurement was carried out in a gas chamber with a quartz transparent window. The concentration of the NO₂ gas was controlled by two mass flow controllers (S49 32/MT). During the measurement, V_{DS} of a periodic sawtooth signal was applied to the FETs with a frequency of 8.3×10^{-3} Hz, and V_{GS} was constant at a specific value. When the gas was off, the FET was illuminated by white light (408 lx, 0.9 mW/cm²) for 1 min to promote the desorption of gas molecules. Supplementary V provides more detailed information on the measurement method.

Supporting Information.

Here, you will find the detailed information for " Characterization of monolayer MoS₂ ", " The output curve of monolayer MoS₂ FET in low V_{DS} regime ", " The NNH fit of the logarithm of

G of $\text{MoS}_{2-0.51}\text{O}_{0.51}$ ", " The avalanche multiplication behavior of pristine MoS_2 FET ", " The detail of measurement method for R_{ADR} ", " The output curve of the $\text{MoS}_{2-0.51}\text{O}_{0.51}$ FET with the continuous decrease of the NO_2 concentration from 50 ppb over time ", " Comparing of the gas-sensing response based on TMDCs ".

ACKNOWLEDGMENT

This work is supported by the National Natural Science Foundation of China (No. 12122508).

REFERENCES

- [1] D. J. Late, Y. K. Huang, B. Liu, J. Acharya, S. N. Shirodkar, J. Luo, A. Yan, D. Charles, U. V. Waghmare, V. P. Dravid, C. N. Rao, Sensing behavior of atomically thin-layered MoS₂ transistors, *ACS Nano* 7 (6) (2013) 4879-4891. <https://doi.org/10.1021/nn400026u>.
- [2] C. Xie, C. Mak, X. Tao, F. Yan, Photodetectors Based on Two-Dimensional Layered Materials Beyond Graphene, *Adv. Funct. Mater.* 27 (19) (2017) 1603886. <https://doi.org/10.1002/adfm.201603886>.
- [3] F. H. Koppens, T. Mueller, P. Avouris, A. C. Ferrari, M. S. Vitiello, M. Polini, Photodetectors based on graphene, other two-dimensional materials and hybrid systems, *Nat. Nanotechnol.* 9 (10) (2014) 780-793. <https://doi.org/10.1038/nnano.2014.215>.
- [4] X. Liu, T. Ma, N. Pinna, J. Zhang, Two-Dimensional Nanostructured Materials for Gas Sensing, *Adv. Funct. Mater.* 27 (37) (2017) 1702168. <https://doi.org/10.1002/adfm.201702168>.
- [5] Q. H. Wang, K. Kalantar-Zadeh, A. Kis, J. N. Coleman, M. S. Strano, Electronics and optoelectronics of two-dimensional transition metal dichalcogenides, *Nat. Nanotechnol.* 7 (11) (2012) 699-712. <https://doi.org/10.1038/nnano.2012.193>.
- [6] D. Jariwala, V. K. Sangwan, L. J. Lauhon, T. J. Marks, M. C. Hersam, Emerging device applications for semiconducting two-dimensional transition metal dichalcogenides, *ACS Nano* 8 (2) (2014) 1102-1120. <https://doi.org/10.1021/nn500064s>.
- [7] S. J. Kim, K. Choi, B. Lee, Y. Kim, B. H. Hong, Materials for Flexible, Stretchable Electronics: Graphene and 2D Materials, *Annu. Rev. Mater. Sci.* 45 (1) (2015) 63-84. <https://doi.org/10.1146/annurev-matsci-070214-020901>.
- [8] J. Pak, Y. Jang, J. Byun, K. Cho, T. Y. Kim, J. K. Kim, B. Y. Choi, J. Shin, Y. Hong, S. Chung, T. Lee, Two-Dimensional Thickness-Dependent Avalanche Breakdown Phenomena in MoS₂ Field-Effect Transistors under High Electric Fields, *ACS Nano* 12 (7) (2018) 7109-7116. <https://doi.org/10.1021/acsnano.8b02925>.
- [9] J. Kim, K. Cho, J. Pak, W. Lee, J. Seo, J. K. Kim, J. Shin, J. Jang, K. Y. Baek, J. Lee, S. Chung, K. Kang, T. Lee, Channel-Length-Modulated Avalanche Multiplication in Ambipolar WSe₂ Field-Effect Transistors, *ACS Nano* 16 (4) (2022) 5376-5383. <https://doi.org/10.1021/acsnano.1c08104>.
- [10] W. Deng, X. Chen, Y. Li, C. You, F. Chu, S. Li, B. An, Y. Ma, L. Liao, Y. Zhang, Strain Effect

- Enhanced Ultrasensitive MoS₂ Nanoscroll Avalanche Photodetector, *J. Phys. Chem. Lett.* 11 (11) (2020) 4490-4497. <https://doi.org/10.1021/acs.jpcllett.0c00861>.
- [11] L. Y. Meng, N. N. Zhang, M. L. Yang, X. X. Yuan, M. L. Liu, H. Y. Hu, L. M. Wang, Low-voltage and high-gain WSe₂ avalanche phototransistor with an out-of-plane WSe₂/WS₂ heterojunction, *Nano Res.* 16 (2022) 3422. <https://doi.org/10.1007/s12274-022-4954-6>.
- [12] H. Choi, S. Choi, T. Kang, H. Son, C. Kang, E. Hwang, S. Lee, Broad-Spectrum Photodetection with High Sensitivity Via Avalanche Multiplication in WSe₂, *Adv. Opt. Mater.* 10 (22) (2022) 2201196. <https://doi.org/10.1002/adom.202201196>.
- [13] B. Son, Y. Wang, M. Luo, K. Lu, Y. Kim, H. J. Joo, Y. Yi, C. Wang, Q. J. Wang, S. H. Chae, D. Nam, Efficient Avalanche Photodiodes with a WSe₂/MoS₂ Heterostructure via Two-Photon Absorption, *Nano Lett.* 22 (23) (2022) 9516-9522. <https://doi.org/10.1021/acs.nanolett.2c03629>.
- [14] J. Seo, J. H. Lee, J. Pak, K. Cho, J. K. Kim, J. Kim, J. Jang, H. Ahn, S. C. Lim, S. Chung, K. Kang, T. Lee, Ultrasensitive Photodetection in MoS₂ Avalanche Phototransistors, *Adv. Sci.* 8 (19) (2021) 2102437. <https://doi.org/10.1002/advs.202102437>.
- [15] F. Ahmed, Y. D. Kim, Z. Yang, P. He, E. Hwang, H. Yang, J. Hone, W. J. Yoo, Impact ionization by hot carriers in a black phosphorus field effect transistor, *Nat. Commun.* 9 (1) (2018) 3414. <https://doi.org/10.1038/s41467-018-05981-0>.
- [16] A. Gao, J. Lai, Y. Wang, Z. Zhu, J. Zeng, G. Yu, N. Wang, W. Chen, T. Cao, W. Hu, D. Sun, X. Chen, F. Miao, Y. Shi, X. Wang, Observation of ballistic avalanche phenomena in nanoscale vertical InSe/BP heterostructures, *Nat. Nanotechnol.* 14 (3) (2019) 217-222. <https://doi.org/10.1038/s41565-018-0348-z>.
- [17] Y. Hattori, T. Taniguchi, K. Watanabe, K. Nagashio, Impact ionization and transport properties of hexagonal boron nitride in a constant-voltage measurement, *Phys. Rev. B* 97 (4) (2018) 045425. <https://doi.org/10.1103/PhysRevB.97.045425>.
- [18] Z. Zhang, B. Cheng, J. Lim, A. Gao, L. Lyu, T. Cao, S. Wang, Z. A. Li, Q. Wu, L. K. Ang, Y. S. Ang, S. J. Liang, F. Miao, Approaching the Intrinsic Threshold Breakdown Voltage and Ultrahigh Gain in a Graphite/InSe Schottky Photodetector, *Adv. Mater.* 34 (47) (2022) 2206196. <https://doi.org/10.1002/adma.202206196>.
- [19] V. K. Sangwan, J. Kang, D. Lam, J. T. Gish, S. A. Wells, J. Luxa, J. P. Male, G. J. Snyder, Z. Sofer, M.

- C. Intrinsic carrier multiplication in layered Bi₂O₂Se avalanche photodiodes with gain bandwidth product exceeding 1 GHz, *Nano Res.* 14 (6) (2020) 1961-1966. <https://doi.org/10.1007/s12274-020-3059-3>.
- [20] S. Lei, F. Wen, L. Ge, S. Najmaei, A. George, Y. Gong, W. Gao, Z. Jin, B. Li, J. Lou, J. Kono, R. Vajtai, P. Ajayan, N. J. Halas, An Atomically Layered InSe Avalanche Photodetector, *Nano Lett.* 15 (5) (2015) 3048-3055. <https://doi.org/10.1021/acs.nanolett.5b00016>.
- [21] J. Jia, J. Jeon, J. H. Park, B. H. Lee, E. Hwang, S. Lee, Avalanche Carrier Multiplication in Multilayer Black Phosphorus and Avalanche Photodetector, *Small* 15 (38) (2019) 1805352. <https://doi.org/10.1002/sml.201805352>.
- [22] S. Das Sarma, S. Adam, E. H. Hwang, E. Rossi, Electronic transport in two-dimensional graphene, *Rev. Mod. Phys.* 83 (2) (2011) 407-470. <https://doi.org/10.1103/RevModPhys.83.407>.
- [23] S. Kc, R. C. Longo, R. Addou, R. M. Wallace, K. Cho, Impact of intrinsic atomic defects on the electronic structure of MoS₂ monolayers, *Nanotechnology* 25 (37) (2014) 375703. <https://doi.org/10.1088/0957-4484/25/37/375703>.
- [24] S. Yuan, R. Roldán, M. I. Katsnelson, F. Guinea, Effect of point defects on the optical and transport properties of MoS₂ and WS₂, *Phys. Rev. B* 90 (4) (2014) 041402. <https://doi.org/10.1103/PhysRevB.90.041402>.
- [25] H. Komsa, J. Kotakoski, S. Kurasch, O. Lehtinen, U. Kaiser, A. V. Krasheninnikov, Two-Dimensional Transition Metal Dichalcogenides under Electron Irradiation: Defect Production and Doping, *Phys. Rev. Lett.* 109 (3) (2012) 035503. <https://doi.org/10.1103/PhysRevLett.109.035503>.
- [26] X. Zhang, L. Gao, H. Yu, Q. Liao, Z. Kang, Z. Zhang, Y. Zhang, Single-Atom Vacancy Doping in Two-Dimensional Transition Metal Dichalcogenides, *Acc. Mater. Res.* 2 (8) (2021) 655-668. <https://doi.org/10.1021/accountsmr.1c00097>.
- [27] Y. Liu, Z. Gao, Y. Tan, F. Chen, Enhancement of Out-of-Plane Charge Transport in a Vertically Stacked Two-Dimensional Heterostructure Using Point Defects, *ACS Nano* 12 (10) (2018) 10529-10536. <https://doi.org/10.1021/acsnano.8b06503>.
- [28] Y. J. Zheng, Y. Chen, Y. L. Huang, P. K. Gogoi, M.-Y. Li, L.-J. Li, P. E. Trevisanutto, Q. Wang, S. J. Pennycook, A. T. S. Wee, S. Y. Quek, Point Defects and Localized Excitons in 2D WSe₂, *ACS Nano* 13 (5) (2019) 6050-6059. <https://doi.org/10.1021/acsnano.9b02316>.

- [29] Z. Yu, Z. Y. Ong, S. Li, J. B. Xu, G. Zhang, Y. W. Zhang, Y. Shi, X. Wang, Analyzing the Carrier Mobility in Transition-Metal Dichalcogenide MoS₂ Field-Effect Transistors, *Adv. Funct. Mater.* 27 (19) (2017) 1604093. <https://doi.org/10.1002/adfm.201604093>.
- [30] L. Li, M.-F. Lin, X. Zhang, A. Britz, A. Krishnamoorthy, R. Ma, R. K. Kalia, A. Nakano, P. Vashishta, P. Ajayan, M. C. Hoffmann, D. M. Fritz, U. Bergmann, O. V. Prezhdo, Phonon-Suppressed Auger Scattering of Charge Carriers in Defective Two-Dimensional Transition Metal Dichalcogenides, *Nano Lett.* 19 (9) (2019) 6078-6086. <https://doi.org/10.1021/acs.nanolett.9b02005>.
- [31] M. G. Stanford, P. R. Pudasaini, E. T. Gallmeier, N. Cross, L. Liang, A. Oyedele, G. Duscher, M. Mahjouri-Samani, K. Wang, K. Xiao, D. B. Geohegan, A. Belianinov, B. G. Sumpter, P. D. Rack, High Conduction Hopping Behavior Induced in Transition Metal Dichalcogenides by Percolating Defect Networks: Toward Atomically Thin Circuits, *Adv. Funct. Mater.* 27 (36) (2017) 1702829. <https://doi.org/10.1002/adfm.201702829>
- [32] F. Ahmed, A. M. Shafi, D. M. A. Mackenzie, M. A. Qureshi, H. A. Fernandez, H. H. Yoon, M. G. Uddin, M. Kuittinen, Z. Sun, H. Lipsanen, Multilayer MoTe₂ Field-Effect Transistor at High Temperatures, *Adv. Mater. Interfaces* 8 (22) (2021) 2100950. <https://doi.org/10.1002/admi.202100950>
- [33] H. Qiu, T. Xu, Z. Wang, W. Ren, H. Nan, Z. Ni, Q. Chen, S. Yuan, F. Miao, F. Song, G. Long, Y. Shi, L. Sun, J. Wang, X. Wang, Hopping transport through defect-induced localized states in molybdenum disulphide, *Nat. Commun.* 4 (1) (2013) 2642. <https://doi.org/10.1038/ncomms3642>
- [34] M. Y. Han, J. C. Brant, P. Kim, Electron Transport in Disordered Graphene Nanoribbons, *Phys. Rev. Lett.* 104 (5) (2010) 056801. <https://doi.org/10.1103/PhysRevB.88.205414>
- [35] J. Y. Kim, I. Kaganovich, H.-C. Lee, Review of the gas breakdown physics and nanomaterial-based ionization gas sensors and their applications, *Plasma Sources Sci Technol.* 31 (3) (2022) 033001. <https://doi.org/10.1088/1361-6595/ac4574>
- [36] S. Bakhshi Sichani, A. Nikfarjam, H. Hajghassem, A novel miniature planar gas ionization sensor based on selective growth of ZnO nanowires, *Sens. Actuator A Phys.* 288 (2019) 55-60. <https://doi.org/10.1016/j.sna.2019.01.024>.
- [37] R. Mohammadpour, H. Ahmadvand, A. Irajizad, A novel field ionization gas sensor based on self-organized CuO nanowire arrays, *Sens. Actuator A Phys.* 216 (2014) 202-206. <https://doi.org/10.1016/j.sna.2014.04.038>.

- [38] J. Zhang, Y. Zhang, Z. Pan, S. Yang, J. Shi, S. Li, D. Min, X. Li, X. Wang, D. Liu, A. Yang, Properties of a weakly ionized NO gas sensor based on multi-walled carbon nanotubes, *Appl. Phys. Lett.* 107 (9) (2015) 093104. <https://doi.org/10.1063/1.4930020>
- [39] P. Abedini Sohi, M. Kahrizi, Low-Voltage Gas Field Ionization Tunneling Sensor Using Silicon Nanostructures, *IEEE Sens. J.* 18 (15) (2018) 6092-6096. <https://doi.org/10.1109/JSEN.2018.2846254>.
- [40] S. Bertolazzi, S. Bonacchi, G. Nan, A. Pershin, D. Beljonne, P. Samori, Engineering Chemically Active Defects in Monolayer MoS₂ Transistors via Ion-Beam Irradiation and Their Healing via Vapor Deposition of Alkanethiols, *Adv. Mater.* 29 (18) (2017) 1606760. <https://doi.org/10.1002/adma.201606760>.
- [41] X. Xiong, F. Wu, Y. Ouyang, Y. Liu, Z. Wang, H. Tian, M. Dong, Oxygen Incorporated MoS₂ for Rectification-Mediated Resistive Switching and Artificial Neural Network, *Adv. Funct. Mater.* (2023) 2213348. <https://doi.org/10.1002/adfm.202213348>.
- [42] D. M. Sim, M. Kim, S. Yim, M.-J. Choi, J. Choi, S. Yoo, Y. S. Jung, Controlled Doping of Vacancy-Containing Few-Layer MoS₂ via Highly Stable Thiol-Based Molecular Chemisorption, *ACS Nano* 9 (12) (2015) 12115-12123. <https://doi.org/10.1021/acs.nano.5b05173>
- [43] A. G. Chynoweth, Uniform Silicon p-n Junctions. II. Ionization Rates for Electrons, *J. Appl. Phys.* 31 (7) (1960) 1161-1165. <https://doi.org/10.1063/1.1735795>.
- [44] K. G. McKay, K. B. McAfee, Electron Multiplication in Silicon and Germanium, *Phys. Rev.* 91 (5) (1953) 1079-1084. <https://doi.org/10.1103/PhysRev.91.1079>.
- [45] B. Cho, M. G. Hahm, M. Choi, J. Yoon, A. R. Kim, Y. J. Lee, S. G. Park, J. D. Kwon, C. S. Kim, M. Song, Y. Jeong, K. S. Nam, S. Lee, T. J. Yoo, C. G. Kang, B. H. Lee, H. C. Ko, P. M. Ajayan, D. H. Kim, Charge-transfer-based gas sensing using atomic-layer MoS₂, *Sci. Rep.* 5 (2015) 8052. <https://doi.org/10.1038/srep08052>.
- [46] S. Y. Cho, S. J. Kim, Y. Lee, J. S. Kim, W. B. Jung, H. W. Yoo, J. Kim, H. T. Jung, Highly Enhanced Gas Adsorption Properties in Vertically Aligned MoS₂ Layers, *ACS Nano* 9 (9) (2015) 9314-9321. <https://doi.org/10.1021/acs.nano.5b04504>.
- [47] D. B. Trivedi, G. Turgut, Y. Qin, M. Y. Sayyad, D. Hajra, M. Howell, L. Liu, S. Yang, N. H. Patoary, H. Li, M. M. Petric, M. Meyer, M. Kremser, M. Barbone, G. Soavi, A. V. Stier, K. Muller, S. Yang, I. S. Esqueda, H. Zhuang, J. J. Finley, S. Tongay, Room-Temperature Synthesis of 2D Janus Crystals

and their Heterostructures, Adv. Mater. 32 (50) (2020) 2006320.!

<https://doi.org/10.1002/adma.202006320>.

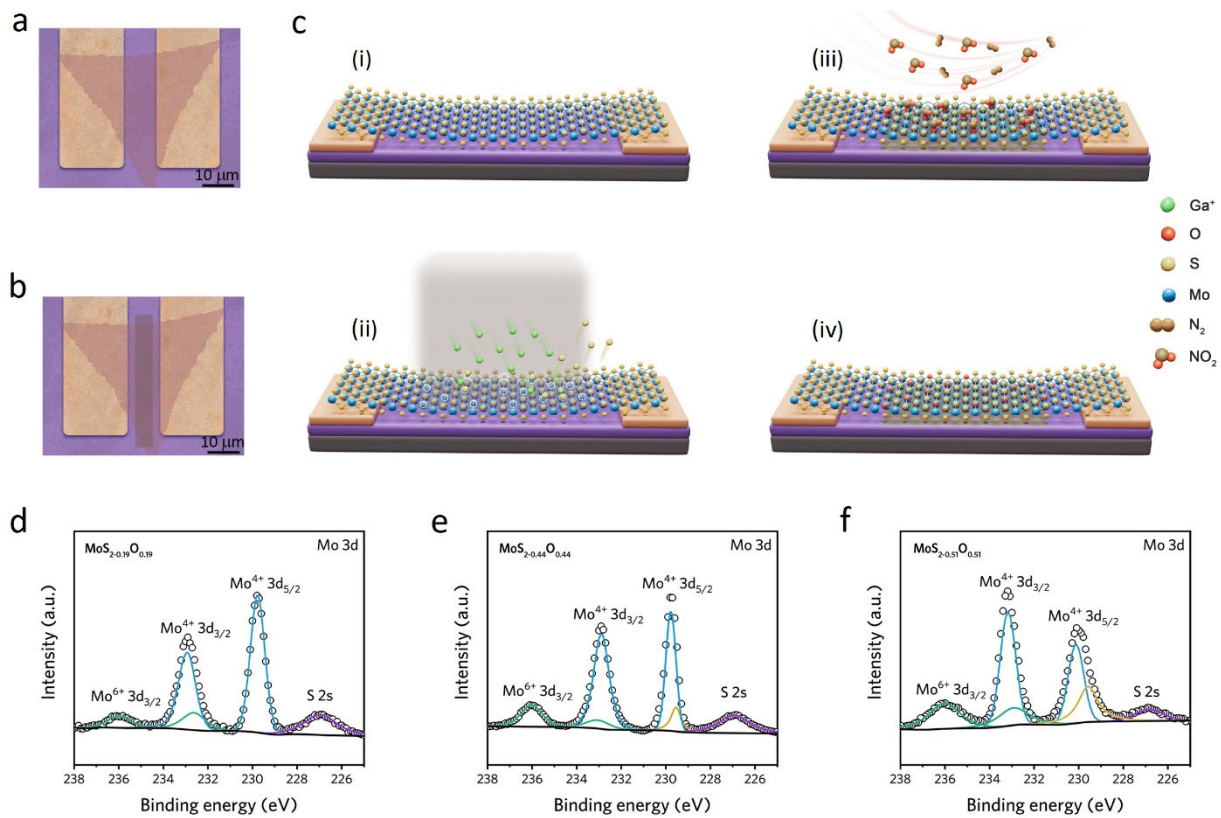


Fig. 1. Preparation of monolayer $\text{MoS}_{2-x}\text{O}_x$. SEM images of the molybdenic sulfide before (a) and after (b) ion irradiation. (c) Preparation process of the $\text{MoS}_{2-x}\text{O}_x$. XPS spectra of $\text{MoS}_{2-0.19}\text{O}_{0.19}$ (d), $\text{MoS}_{2-0.44}\text{O}_{0.44}$ (e), and $\text{MoS}_{2-0.51}\text{O}_{0.51}$ (f).

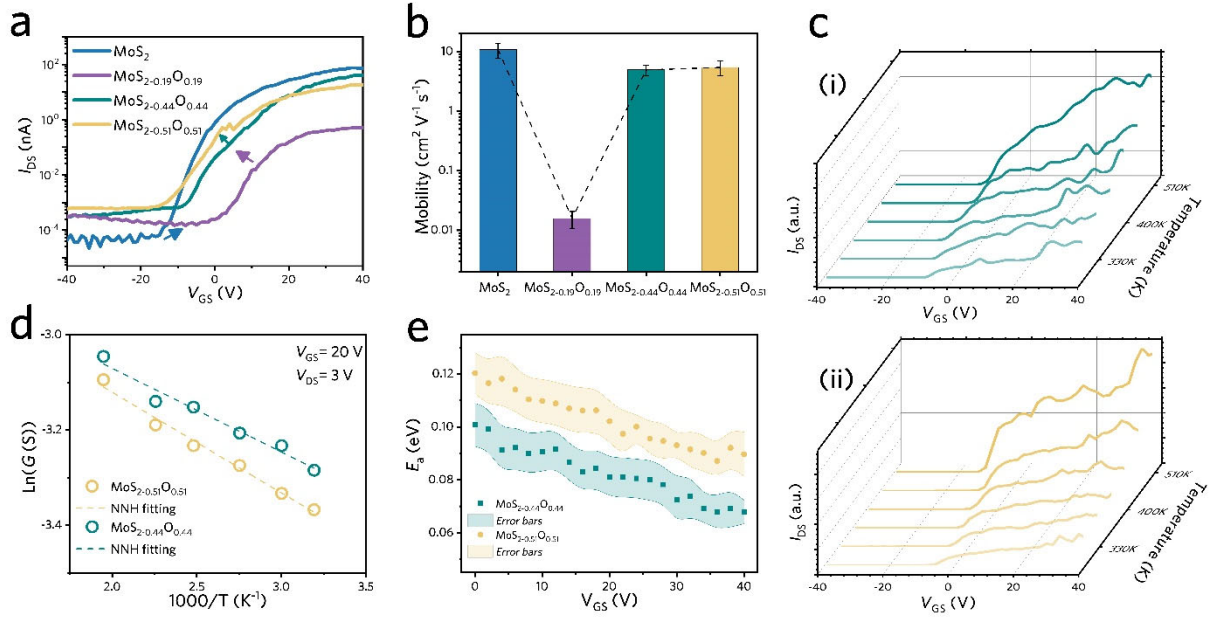


Fig. 2. NNH transfer behavior in monolayer $\text{MoS}_{2-x}\text{O}_x$. **(a)** Transfer characteristics of MoS_2 and $\text{MoS}_{2-x}\text{O}_x$ ($x = 0.19, 0.44$ and 0.51) at room temperature, presented in the logarithmic scale. **(b)** Mobility variation of $\text{MoS}_{2-x}\text{O}_x$ corresponding to x . **(c)** variation of $I_{DS}-V_{GS}$ curves ($V_{DS}=3\text{V}$) for $\text{MoS}_{2-0.44}\text{O}_{0.44}$ (i) and $\text{MoS}_{2-0.51}\text{O}_{0.51}$ (ii) as the temperature increases from 310 K to 510 K. **(d)** The linear fit of the logarithm of G as a function of T^{-1} . **(e)** Relationship between E_a and V_{GS} .

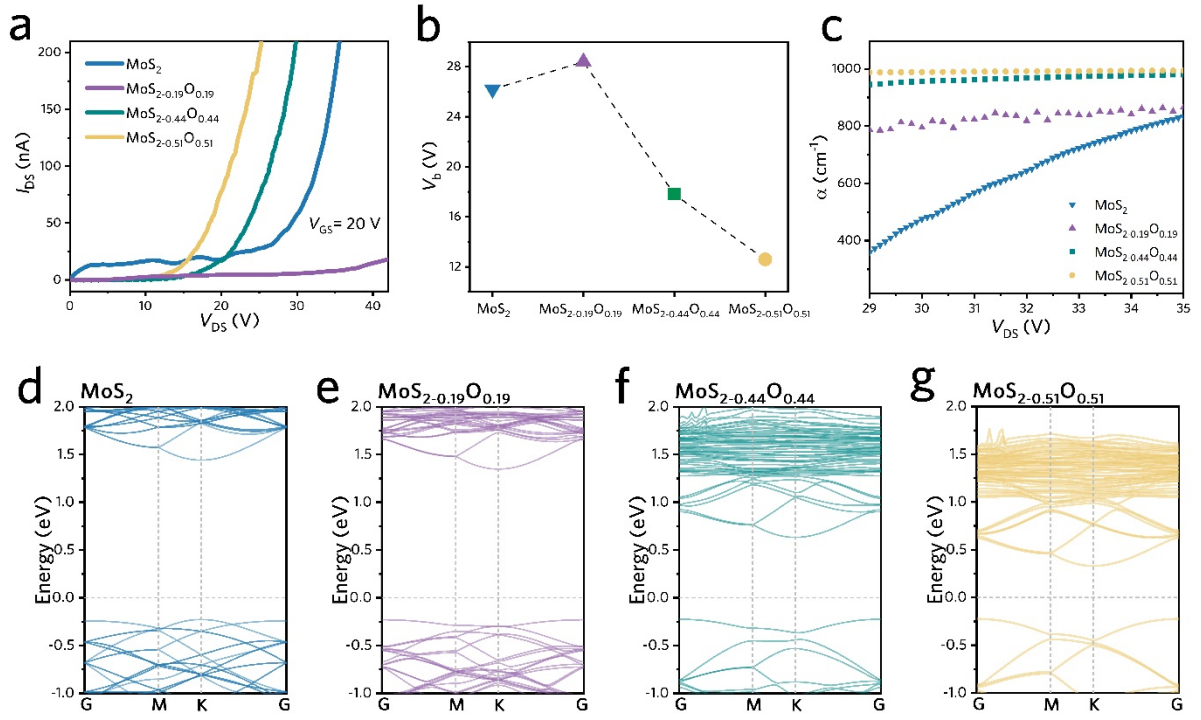


Fig. 3. Avalanche characterization of monolayer $\text{MoS}_{2-x}\text{O}_x$. **(a)** $I_{\text{DS}}-V_{\text{DS}}$ curves of $\text{MoS}_{2-x}\text{O}_x$ FET with a fixed V_{GS} of 20 V. **(b)** V_{b} of $\text{MoS}_{2-x}\text{O}_x$. **(c)** Variation of α with V_{DS} . Electronic structures of MoS_2 **(d)**, $\text{MoS}_{2-0.19}\text{O}_{0.19}$ **(e)**, $\text{MoS}_{2-0.44}\text{O}_{0.44}$ **(f)**, and $\text{MoS}_{2-0.51}\text{O}_{0.51}$ **(g)**.

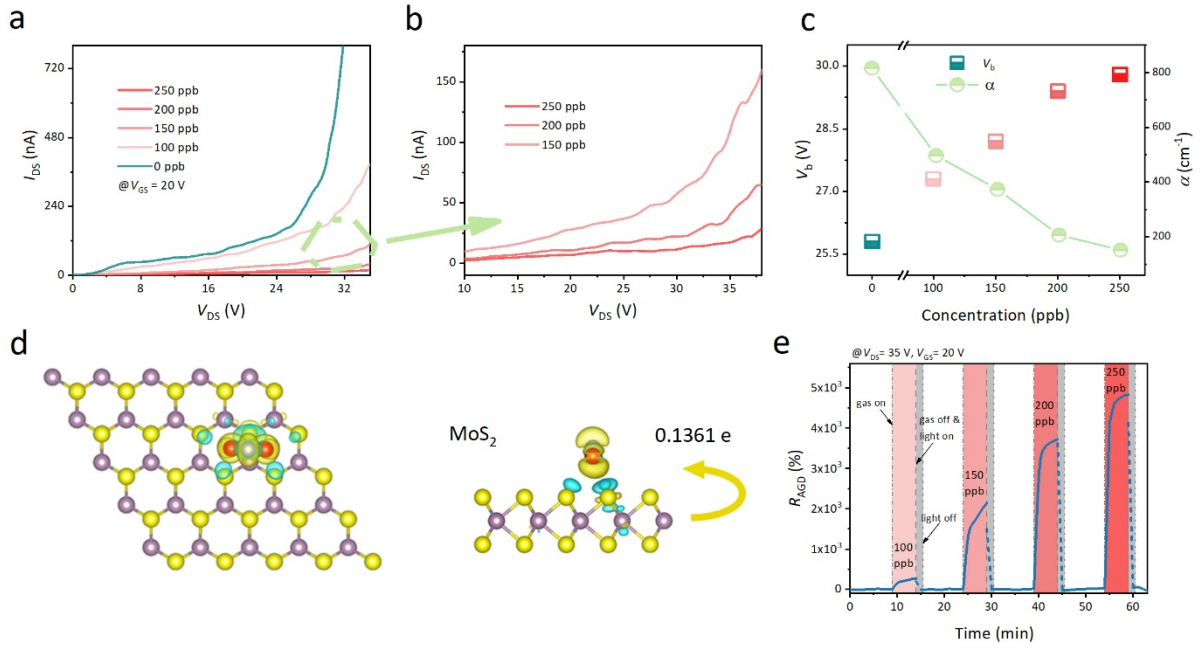


Fig. 4. Gas response of MoS₂ FET with NO₂ adsorption. (a) I_{DS} - V_{DS} curves of a monolayer MoS₂ FET at $V_{GS} = 20$ V in ambient air and various concentrations of NO₂ ranging from 100 ppb to 250 ppb with a step of 50 ppb. (b) A larger view of the portion in green box shown in (a). (c) V_b and α ($V_{DS} = 35$ V) values at $V_{GS} = 20$ V in different gas atmospheres, represented as balls and squares, respectively. (d) Calculated charge transfer of MoS₂ FET with NO₂ adsorption. (e) Measurements of avalanche gas detection response (R_{ADR}) in different gas atmospheres, following the one described in Section *Gas-detecting method*.

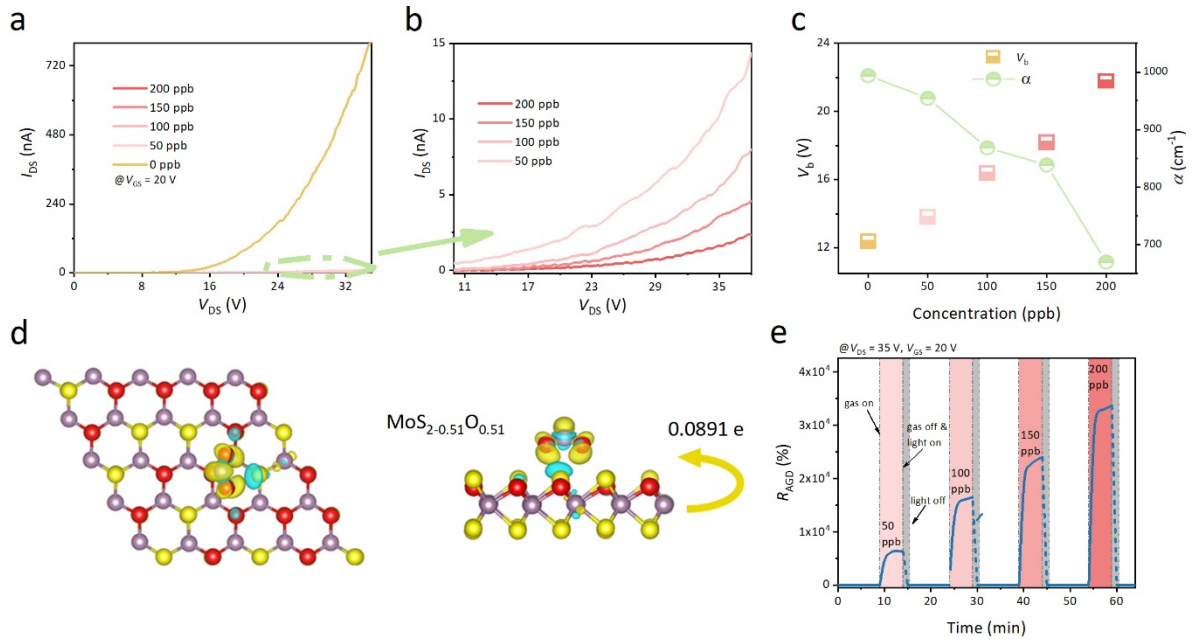


Fig. 5. Gas response of MoS_{2-0.51}O_{0.51} FET with NO₂ adsorption. **(a)** I_{DS} - V_{DS} curves of MoS_{2-0.51}O_{0.51} FET at $V_{GS} = 20$ V in ambient air and various concentrations of NO₂ ranging from 50 ppb to 200 ppb with a step of 50 ppb. **(b)** A larger view of the portion in green box shown in **(a)**. **(c)** V_b and α ($V_{DS} = 35$ V) values at $V_{GS} = 20$ V in different gas atmospheres, respectively. **(d)** Calculated charge transfer of MoS_{2-0.51}O_{0.51} FET with NO₂ adsorption. **(e)** Measurements of avalanche gas detection response (R_{ADR}) in different gas atmospheres, following the one described in Section *Gas-detecting method*.